ORIGINAL PAPER

Thickness accuracy of virtually designed patient-specific implants for large neurocranial defects

Claudia Wittner[1] | Markus Borowski[2] | Lukas Pirl[2] | Johann Kastner[1] | Andreas Schrempf[3] | Ute Schäfer[4] | Klemens Trieb[1,5] | Sascha Senck[1]

[1]Research Group Computed Tomography, University of Applied Sciences Upper Austria, Wels, Austria

[2]Institut für Röntgendiagnostik und Nuklearmedizin, Städtisches Klinikum Braunschweig GmbH, Braunschweig, Germany

[3]Research Group for Surgical Simulators Linz, University of Applied Sciences Upper Austria, Linz, Austria

[4]Forschungseinheit Experimentelle Neurotraumatologie, Medizinische Universität Graz, Graz, Austria

[5]Department of Orthopedic and Trauma Surgery, Paracelsus Medical University Salzburg, Salzburg, Austria

Correspondence
Sascha Senck, University of Applied Sciences Upper Austria, Stelzhamerstraße 23, 4600 Wels, Austria.
Email: sascha.senck@fh-wels.at

Funding information
European Union's Horizon 2020 Program; K-Project for "Photonic Sensing for Smarter Processes", Grant/Award Number: 871974; CAMed, Grant/Award Number: 871132; Federal Ministry Republic of Austria Climate Action, Environment, Energy, Mobility, Innovation and Technology (BMK); Federal Ministry Republic of Austria Digital and Economic Affairs (BMDW); Styrian Business Promotion Agency (SFG)

Abstract

The combination of computer-aided design (CAD) techniques based on computed tomography (CT) data to generate patient-specific implants is in use for decades. However, persisting disadvantages are complicated design procedures and rigid reconstruction protocols, for example, for tailored implants mimicking the patient-specific thickness distribution of missing cranial bone. In this study we used two different approaches, CAD- versus thin-plate spline (TPS)-based implants, to reconstruct extensive unilateral and bilateral cranial defects in three clinical cases. We used CT data of three complete human crania that were virtually damaged according to the missing regions in the clinical cases. In total, we carried out 132 virtual reconstructions and quantified accuracy from the original to the generated implant and deviations in the resulting implant thickness as root-mean-square error (RMSE). Reconstructions using TPS showed an RMSE of 0.08–0.18 mm in relation to geometric accuracy. CAD-based implants showed an RMSE of 0.50–1.25 mm. RMSE in relation to implant thickness was between 0.63 and 0.70 mm (TPS) while values for CAD-based implants were significantly higher (0.63–1.67 mm). While both approaches provide implants showing a high accuracy, the TPS-based approach additionally provides implants that accurately reproduce the patient-specific thickness distribution of the affected cranial region.

KEYWORDS
computer-aided design, cranial flap, craniofacial defects, implant design, thin-plate splines

1 | INTRODUCTION

Bone loss due to cranial trauma, disease or accidents requires an adequate treatment including craniofacial reconstruction, for example, using additive manufacturing (AM; Msallem et al., 2017). Special care is required for the design and manufacturing process of cranial implants since a gap between bone and implant might act as a route for infections (Rotaru et al., 2012). Functional deficiencies occurring in patients with cranial defects may lead to trephination syndrome (sinking skin flap syndrome) characterized by dizziness, irritability or intolerance to noise (Bonda et al., 2015). Besides functional reasons, aesthetics is the most important aspect for the patient in

relation to psyche and social life. Cranioplasty is an effective way to treat cranial defects, e.g., in relation to the trephination syndrome in order to improve neurological functions (Mokri, 2010). Virtually designed implants in combination with computer-assisted surgery (CAS) represent advanced surgical procedures to support the treatment process. Several studies showed that preoperative selection of prosthesis design and additively manufactured templates positively influence the outcome in relation to accurate bone removal, faster surgical procedures, and accuracy of implant placement (Chamo et al., 2020; Jones, 2013; Bonda et al., 2015).

Various software tools emerged in the last decades supporting virtual implant design. Commercial software like Materialise Mimics®, Biobuild or 3D DOCTOR provide various methods for cranial reconstruction. However, expert knowledge in computer-aided design (CAD) is a general precondition during cranial reconstruction and implant design. Additionally, a potential disadvantage of commercially available software is that the underlying algorithms and procedural steps during implant design often cannot be traced (black-box scenario) (Egger et al., 2017). This is true for available software packages operated by clinicians, but also for external commercial services that are designing implants based on provided medical CT data from a hospital. A major shortcoming in the use of external services in clinical practices can be the lack of a detailed step-by-step documentation of implant design. Hence, a measure for the accuracy of the provided virtual implant model and consequently for the physical implant is missing. This concerns both the geometric accuracy and the accuracy in relation to the thickness of the generated implant.

In general, the restoration of cranial morphology is a challenging task particularly if large defective areas are involved. Conventional reconstruction methods such as mirror imaging the healthy, unaffected cranial side are not applicable for bilateral cases with (partly) missing midsagittal planes (Egger et al., 2017; Fuessinger et al., 2018; Klammert et al., 2010; Truscott et al., 2007). Moreover, since every cranium is characterized by a certain degree of asymmetry, mirror imaging can lead to large deviations of affected regions during alignment of the affected and unaffected side (Quinto-Sánchez et al., 2015). Alternatively, deformation-based geometric morphometrics (GM) show a high potential for the generation of patient-specific implants, since available morphological information of the reconstructed cranium is incorporated into the final implant (Marreiros et al., 2016; Mitteroecker & Gunz, 2009; Senck et al., 2013). Using thin-plate splines (TPS), a mapping function warps the landmark configuration (template) from a complete reference specimen onto a target specimen showing cranial defects (Bookstein, 1989). Hence, in addition to optimizing geometric accuracy, that is, shape, spatial variation in implant thickness is considered in the final implant design when using internal and external cranial landmarks in the template.

The suitability of the respective reconstruction approach depends on location, defect size, and available resources. Benazzi and Senck (2011) showed that the TPS reconstruction of craniomaxillofacial defects is more precise compared to mirroring technique. The evaluation of standard deviation and mean showed significant differences between the two approaches. Additionally, they showed that asymmetric hemifaces negatively influence the accuracy of the mirror imaging approach (Benazzi & Senck, 2011). The same trend was shown by Fuessinger et al. (2018) in a comparative reconstruction analysis of large cranial defects, determining significant higher accuracy (mean error) for the geometric reconstruction using the statistical mean shape as reference, compared to mirror imaging. By combining GM and radial basis function, Marreiros obtained a mean error less or equal to 1 mm for the reconstruction of large cranial defects (>100 cm^2) (Marreiros et al., 2016).

Using AM, virtual models can directly be transferred to physical representations, for example, for the purpose of preoperative planning, or directly for the generation of final implants. In the latter case, error propagation can lead to large deviations if the process capability of AM systems and materials are not compatible with specified tolerances. For example, Brown compared two 3D printers which both produce clinically acceptable models with high accuracy (Brown et al., 2018) according to an acceptable range (0.20–0.50 mm deviation) reported in several studies (Halazonetis, 2001; Hassan et al., 2017; Hazeveld et al., 2014; Schirmer & Wiltshire, 1997; Sohmura et al., 2001).

Besides implant planning and design, material choice and implant thickness influence the outcome of every cranial reconstruction. Each material shows a specific combination of properties like biocompatibility, bioactivity, toxicity, yield strength, and implanting complexity (Kwarcinski et al., 2017). In general, the adequate manufacturing process has to be chosen in accordance with the employed material. For instance, not all potential implant materials are suitable for AM. Common implant materials are polymethylmethacrylate (PMMA), polyetheretherketone (PEEK), polyethylene, hydroxyapatite, and titanium (Kwarcinski et al., 2017). PEEK delivers the most satisfactory results for large-sized cranial defects, especially considering its physical and mechanical characteristics (strength, stiffness, durability) and its suitability for 3D printing (Mohan et al., 2016; Petersmann et al., 2019). PMMA is characterized by its obtainability, processability, and affordability, rendering it one of the most frequently used materials for implant design. Compared to polylactide and acrylonitrile butadiene styrene, PMMA is also suitable for long-term use (Petersmann et al., 2019). Long-term reliability is influenced by factors like defect location and shape, bone quality, expected loads, and constraints caused by the surrounding soft tissue.

Statistical assessment revealed that the implant material predominantly influences deflection. In contrast, implant peak stresses are primarily caused by implant thickness distribution (Marcián et al., 2019). Adequate consideration of these two factors—material and thickness—in addition to geometric accuracy influence implant performance and its ability to mimic bone biomechanical behavior. However, as noted by Persson et al. (2018), PEEK is still the preferred material choice to mimic the mechanical response and native behavior of the cranium. PEEK and PMMA are preferred implant materials, as they can be easily adapted to the current bone structure in the operating theatre. In general, the decision of material and thickness still depends on quality of the

patient's native bone and is thus patient-specific. This highlights the importance of the collaboration between medical engineers designing implants and the surgeon to choose the appropriate combination of material and thickness in patient-specific implants (Ladaru et al., 2019).

In this study, we virtually reconstructed three clinical cases and corresponding artificially damaged knockout (KO) individuals with large-sized bilateral and unilateral defects. A geometric, reference-based reconstruction approach is compared to implants created in a designated design workflow in a common CAD software which offers built in reconstruction techniques. Geometric reconstruction accuracy is evaluated by means of root-mean-square error (RSME). Additionally, we provide information on the accuracy of virtual models in relation to bone thickness and visualize thickness distributions of generated CAD- and TPS-based implants. This is the first analysis comparing two different approaches including external as well as internal morphological information for the reconstruction of large cranial implants.

2 | MATERIALS AND METHODS

2.1 | Samples

Clinical computed tomography (CT) scans were acquired between 2010 and 2016 at the Klinikum Braunschweig. Written consent for participation was acquired from all patients. All CT scans were recorded in DICOM file format at a reconstruction matrix size of 512 × 512 pixels with slice thicknesses ranging from 0.5 to 0.6 mm using a Siemens Somatom 16. Clinical case 1 (C1) is characterized by a bilateral defect of approx. 111.25 cm^2 including the bregma region as well as large parts of the frontal bone. The defect extends almost symmetrically to both lateral sides affecting parts of the *sutura coronalis*. The temporal lines are unaffected. The missing areas of the unilateral cases (C2 and C3) include parts of *Os parietale*, *Os frontale*, *Os sphenoidale*, and *Os temporale* including the temporal line. Both defects are located on the right cranial side extending over an area of approx. 93.91 cm^2 (C2) and 127.58 cm^2 (C3) respectively.

The reference sample for the TPS-based approach comprises CT scans of 20 specimens housed at the University of Vienna (Department of Evolutionary Anthropology), see Senck et al. (2013) for details.

2.2 | TPS-based approach

2.2.1 | Landmark template

The TPS approach includes information about the internal and external aspects of the cranial surface (see Figure 1). We used Avizo 9.7 software to create a 3D landmark template (*n* = 831) involving anatomical landmarks (*n* = 47; see Table 1). In addition, we defined curve landmarks along the temporal line (blue), superior half of the
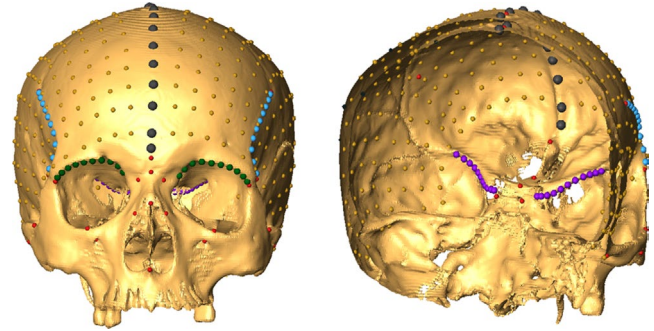

FIGURE 1 Landmark template showing anatomical landmarks (red) and semilandmarks on the external and internal aspects of the cranial vault [Colour figure can be viewed at wileyonlinelibrary.com]

orbit (green), the ala minor (endocranial; purple), as well as the mid-sagittal plane (black). Surface semilandmarks were defined on the external and internal tables of the cranial vault (yellow). The complete landmark template in Figure 1 features anatomical landmarks (red), curve landmarks, and surface semilandmarks.

2.2.2 | Semilandmark warping

The template serves as a reference to warp all semilandmarks onto each target specimen by iterative TPS, using Edgewarp 3D software (Bookstein & Green, 1994). This procedure is based on a mapping function, using smooth interpolation between two points for exact landmark warping (Bookstein & Green, 1993).

Loading the reference and target landmark configuration into Edgewarp 3D performs an affine transformation based on the anatomical landmarks. The warping procedure relies on homologous landmarks, that is, the anatomical landmarks defined in Table 1. The specimen's alignment due to anatomical landmarks represents a first estimation of the final landmark distribution. Repeating the following steps in Edgewarp 3D results in a target landmark configuration showing minimal bending energy: (1) relax specimen against reference, (2) project all semilandmarks, and (3) orient and relax all semilandmarks. The steps are repeated until the optimization criteria of minimal bending energy is below an a priori defined threshold (bending energy change: <0.001) (Marreiros et al., 2016; Mitteroecker & Gunz, 2009; Senck et al., 2013). Misplaced projected semilandmarks at the inner and outer bone surfaces of the surface file representing each specimen were corrected manually.

2.2.3 | Virtual knockout

Based on the available anatomical landmarks of the clinical cases, three of the reference specimens are used as KO individuals. The distance between two sets of Procrustes shape coordinates is referred to as Procrustes distance and denotes (dis)-similarities in shape (Mitteroecker & Gunz, 2009). The specimen with minimal Procrustes distance to the corresponding clinical case was therefore

TABLE 1 List of anatomical landmarks for 3D template

N	Unpaired landmarks	N	Paired landmarks
1	Glabella	2	Frontomalare–temporale
5	Nasale	3	Frontomalare–orbitale
8	Rhinion	4	Frontale/Nasale/Maxillare
10	Bregma[a]	6	Zygoorbitale
16	Lambda[a]	7	Sutura nasomaxillaris
17	Inion[a]	9	Foramen infraorbitale
19	Opisthion[a]	11	Stephanion[a]
21	Jugum sphenoidal mid	12	Zygotemporale superior
22	Os sphenoidal mid hits os etmoidale mid	13	Zygotemporale inferior
25	Anterior cribiform plate	14	Auriculare
		15	Linea temporalis posterior[a]
		18	Foramen ovale anterior
		20	Processus clinoideus posterior
		23	Foramen ovale posterior
		24	Palate canal superior

[a]Landmarks placed on tabula interna and externa.

TABLE 2 Sample list indicating reference individuals S1, S2, and S3 serving as knockout individuals (KO1, KO2, and KO3) and the corresponding clinical cases (C1, C2, and C3)

Reference individual	Clinical cases	Knockout
Specimen 1* (S1)	Clinical case 1* (C1)	Knockout 1* (KO1)
Specimen 2** (S2)	Clinical case 2** (C2)	Knockout 2** (KO2)
Specimen 3*** (S3)	Clinical case 3*** (C3)	Knockout 3*** (KO3)

defined as KO individual for the respective clinical case (S1: complete cranium most similar to clinical case C1, S2:C2, S3:C3; see Table 2) and artificially damaged subsequently.

In order to generate virtual defects, landmarks located in defective areas of the clinical cases (C1, C2, C3) are defined as missing in the respective KO individual (KO1 based on S1, KO2 based on S2, KO3 based on S3). Figure 2a depicts missing landmarks in KO3, the clinical case characterized by the largest cranial defect. Figure 2b shows the corresponding clinical case C3 and the actual cranial defect.

2.2.4 | Geometric reconstruction

Missing data in the KO individuals (KO1, KO2, KO3) and the clinical cases (C1, C2, C3) were estimated by TPS interpolation using a reference sample. The basic concept is to use the mapping function in Edgewarp 3D to warp a complete reference landmark configuration (reference specimen, template) onto an incomplete target (KO individual, clinical case). The semilandmark warping procedure focuses on minimizing the bending energy between reference and target, consequently generating the smoothest interpolation (Bookstein, 1989; Mitteroecker & Gunz, 2009; Senck et al., 2013; Zachow, 2015). Complete reference specimens (n = 20 and the Procrustes mean shape [PMS]) were warped onto each KO individual (KO1, KO2, KO3) and clinical case (C1, C2, C3) respectively. This procedure generates 21 individual geometrical reconstructions for each KO individual and clinical case, that is, a total of 126 geometric reconstructions were created.

2.3 | CAD-based reconstruction

The applied reconstruction pipeline is based on a protocol from a Materialise® workshop (Materialise, 2018):
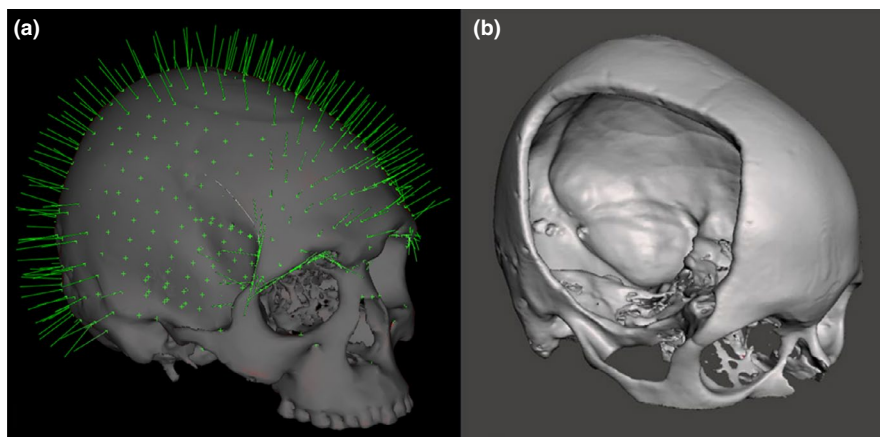

FIGURE 2 Knockout individual (KO3) versus clinical case (C3): (a) landmarks declared missing (cross) and sliding semilandmarks (cross and surface normal), and (b) actual clinical case featuring an extensive unilateral cranial defect extending over an area of 127.58 cm² [Colour figure can be viewed at wileyonlinelibrary.com]
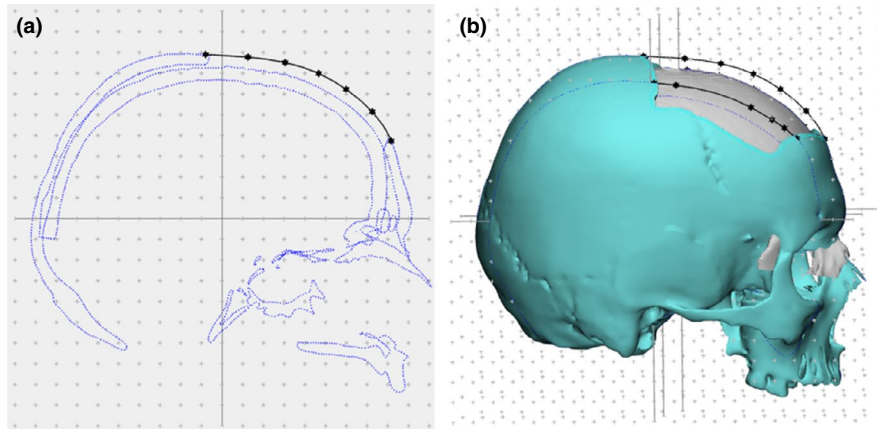
FIGURE 3 Spline drawing for the bilateral defect along the midsagittal plane: (a) outline import of damaged cranium (KO1) and reference (Procrustes mean shape [PMS]); (b) damaged cranium (KO1) with PMS (gray) reference and finished splines [Colour figure can be viewed at wileyonlinelibrary.com]

1. CT—Data processing: segmentation of CT scans and creation of STL files.
2. Reconstruction process: involves mirror imaging techniques and splines.
3. Implant design and post-processing steps including undercut removal and edge smoothing.

Firstly, the area of interest is defined by drawing a curve around the defect. A curvature analysis can help to identify and bypass areas with high stress values. However, in order to define splines, references are required. In case of the unilateral defects, we used mirror imaging to project the unaffected side along the midsagittal plane to generate a mirror image which serves as a template (Fuessinger et al., 2018; Klammert et al., 2010; Moiduddin et al., 2017; Singare et al., 2009). In the bilateral case, mirroring is inapplicable necessitating the usage of a reference cranium. Hence, we used a STL file of the PMS (STL surface generated in Avizo 9.7; scaled by centroid size) as reference to prevent the incorporation of subject-specific anatomical features in the CAD-based reconstruction process. However, the PMS needs manual placement below the defect to cover the transition area, which represents a potential error source and reduces reproducibility of this approach. A second source of error is the size difference between the reference and damaged specimen, as shown in Figure 3.

The outlines of the damaged cranium and the reference are imported into a sketch producing an overlay with an estimation of start and endpoint of the spline. Each spline is subsequently manually drawn on the basis of the reference geometry on the outer bone surface (see Figure 3). The PMS acts as a reference but only defines the shape of the spline due to obvious size differences. Three splines were used in case of the KO1 reconstruction (along midsagittal plane and one each beside). The curve outlining the defect and splines are the base geometries to create a virtual cranial plate. Bone thickness is measured manually around the defect. Measured thickness values are applied to the plate via the variable offset module transforming it into a preliminary virtual implant. Finally, undercuts were removed and a smoothing of the edges was carried out to improve the fitting

of the implant. In total, six CAD-based reconstructions were created (each one reconstruction for C1, C2, C3 and KO1, KO2, KO3). Firstly, the clinical cases were reconstructed to obtain a template for the KO individuals. Subsequently, the outline of the implants of C1, C2, and C3 was projected onto each corresponding cranium (S1, S2, and S3) removing the corresponding defect area by means of Boolean subtraction. Finally, each KO individual (KO1, KO2, KO3) was reconstructed using the steps described above.

2.4 | Statistical analysis

Landmarks and semilandmarks of the created reconstructions (CAD- and TPS-based) were transformed into shape coordinates by generalized Procrustes analysis (GPA). Procrustes superimposition involves translating, rescaling, and rotating landmark configurations relative to each other in order to minimize the sum of squared distances. These shape coordinates are the input for a subsequent principal component analysis (PCA) in shape space. The reconstructions are projected into the original PCA space of the 20 reference specimens to preserve the initial geometrical relationship. Minimal and maximal principal component (PC) scores for the first three PCs were extracted to generate surface morphs in Avizo 9.7.

The visualized 3D shape variation helps in the interpretation of geometrical deviations of the reconstructions with respect to the employed reference specimen, that is, the effect of reference choice (Senck et al., 2015). R provides packages like morpho, which allows, for example, the use of semilandmarks and surface morphs (R Core Team, 2013; Schlager, 2017). GM and statistical procedures such as GPA and PCA were carried out in R.

2.5 | Geometric accuracy (shape)

In the statistical analysis, we only considered the subset of landmarks in the corresponding implant region. Accuracy was

computed as the square root of the average of squared errors (RMSE), that is, the deviation between the original and reconstruction in the respective KO series. Reconstruction accuracy expressed as RMSE is computed to assess the geometric accuracy of each virtually generated implants and has the same units as the original data (mm). The RMSE was computed separately for each reconstruction only including (semi)landmarks located in the implant specific area of the respective KO series (KO1: 78, KO2: 142, KO3: 156 missing landmarks).

We used the software open_iA (Fröhler et al., 2019) to quantify the projected distance from the estimated landmark coordinates in Edgewarp 3D to the bone surface of the corresponding complete cranium (S1, S2, S3). The computation is based on the determination of the surface normal vector. Surface distances, i.e. residual values, are defined as the vector starting from the origin of the estimated landmark to the first intersection point with the bone surface of the reference individual. These residual values were computed for every KO reconstruction (KO1, KO2, KO3; predicted values) and the original crania (S1, S2, S3; observed values). Finally, an averaging was performed over all residuals in the implant specific area for each KO reconstruction (see Tables S1 and S2). This average residual represents the accuracy in the respective implant area for each reconstruction in the training data allowing a comparison of the performance between CAD- and TPS-based implant design approaches.

Geometrical accuracy was additionally visualized in Geomagic Qualify (3D Systems) using a nominal–actual comparison from the complete cranium (S1, S2, S3) to the corresponding KO reconstruction (KO1, KO2, KO3) using the PMS as reference. We compare those results with CAD-based reconstructions carried out in Materialise–3–matic®. A color-coded map indicates negative and positive deviations in the implant area. A comprehensive description is available in Wittner (2019).

2.6 | Implant thickness accuracy

Cranial vault thickness of the complete specimens and each reconstructed cranial implant was computed based on extracted surface data (STL) in open_iA (Fröhler et al., 2019). Thickness values are determined for landmarks that are situated in the implant specific area. Surface thickness is defined as the distance between the first and second intersection of the normal vector of the respective surface semilandmark with the STL surface. Thickness values were computed for each reconstruction (predicted values) and the respective original crania (observed values) in order to compute the RMSE. The thickness RMSE averages all deviations in the respective implant area and indicates thickness deviations from the original cranium for each reconstruction. A comprehensive description of this approach is available in Wittner (2019).

Wall thickness analyses were carried out in Materialise 3-matic® based on generated surface data (STL) and minimal Euclidean distance approach. Thickness distributions were visualized for each PMS- and CAD-based reconstruction (predicted values) and the

respective original crania (observed values). Visualizations feature a color-coded map that indicates the bone thickness distribution of each designed cranial flap for KO1–KO3 and the corresponding clinical cases C1–C3. The thickness maps display the transition area of bone and implant as well as the thickness distribution of the implant itself.

3 | RESULTS

3.1 | Principal components analyses

Figure 4 shows shape differences of the reference sample (20 specimens) along the first three PCs facilitating the interpretation of different reconstruction results. The first three PCs describe approximately 66% of total shape variation. Minimal scores on the left side of PC1 show a narrow and high vaulted cranium whereas maximal PC1 scores correspond to broad and less high crania. Hence, PC1 (43.64%) predominantly characterizes dolichocephalic (minimal scores) versus brachycephalic (maximal scores) cranial shape differences. A broad and stout cranium indicates maximal PC1 scores.

PC2 scores indicate differences in the temporal line and the degree of postorbital constriction. The temporal line runs upwards, the constriction is less pronounced and the cranial vault is higher for low PC2 scores. The visualization of high PC2 scores displays a temporal line characterized by a stronger curvature while the cranium is more globular. Minimal PC3 scores correspond to a globular cranium and a
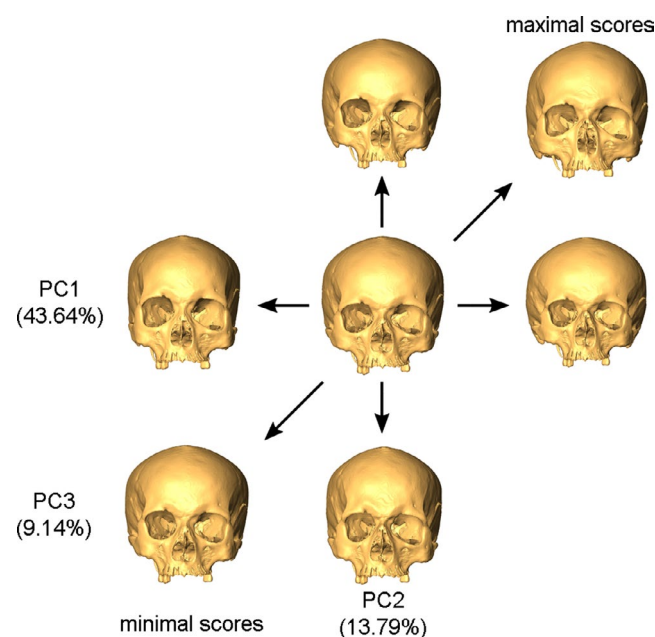

FIGURE 4 Cranial shape variation in the reference sample. The central shape represents the Procrustes mean shape, while the rest of the surface morph represents the respective minima and maxima of the first three principal components (PCs) [Colour figure can be viewed at wileyonlinelibrary.com]

decreased facial width. Maximal PC3 scores mainly correspond to a difference in neurocranial breadth.

KO and clinical case (C) reconstructions were projected into the original shape-space PCA (gray spheres) of the reference specimens. Figure 5 shows the PCA of all bilateral reconstructions (KO1 and C1) while Figure 6 depicts all reconstructions of the unilateral cases KO2/C2 and KO3/C3. S1 to S3 represent the original, complete crania that were used for the definition of KO1 to KO3 respectively. In total, 21 TPS-based reconstructions and one CAD-based reconstruction were generated for each case.

In both PC analyses, the PMS reconstruction of KO1, KO2, and KO3 plot closely to the original cranium (S1, S2, and S3 respectively). The rest of the TPS-based reconstructions form an elliptical posterior distribution of reconstruction around the complete, original cranium. Major shape differences in the KO1 reconstruction, showing a bilateral cranial defect, are related to PC2 that explains approx. 14% of shape variation (see Figure 4). The CAD-based reconstruction of

KO1 is well within the 95% ellipse of the TPS-based reconstructions. However, it plots at the outer border of the distribution showing high positive PC1 scores. Shape variation in the reconstruction of the clinical case C1 is slightly higher, represented by an elongated 95% ellipse along PC2. As expected, the PMS reconstructions plot in the center of the posterior distribution of both KO1 and C1 reconstructions.

Major shape differences in the reconstruction of KO2 and KO3 that display large lateral cranial missing areas are mainly related to PC2 and PC3. Analogously to the bilateral reconstruction, the respective PMS reconstruction plots closely to the complete cranium S2 and S3. In contrast, both CAD-based reconstructions plot outside or on the edge of the 95% confidence interval, predominantly showing higher PC2 and PC3 scores compared to the TPS-based reconstructions. This corresponds to shape differences in relation to the degree of post-orbital constriction and neurocranial width in the CAD-based reconstructions, both affected by the missing unilateral
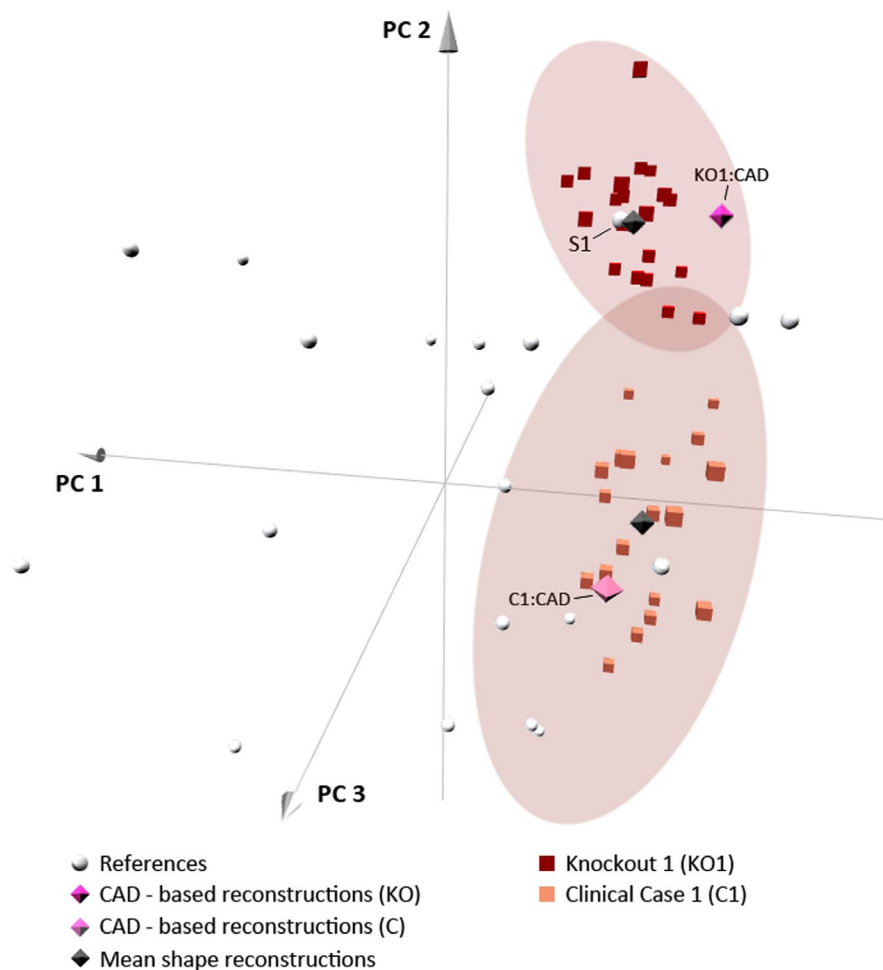

FIGURE 5 Principal component (PC) analysis plot showing the distribution of reconstructions and the corresponding 95% confidence intervals (clinical cases: light-colored squares; knockout individual: dark-colored squares) projected into the shape-space of the reference sample (gray spheres). The reconstruction on the basis of the Procrustes mean shape (black diamond) plots closely to the original, complete specimen (S1). The computer-aided design (CAD)-based reconstruction using Materialise® (magenta diamond) plots in the 95% confidence interval but is on the border of the distribution of reconstructions. The reconstruction of C1 shows a similar pattern but is characterized by a larger shape variation than in KO1 [Colour figure can be viewed at wileyonlinelibrary.com]
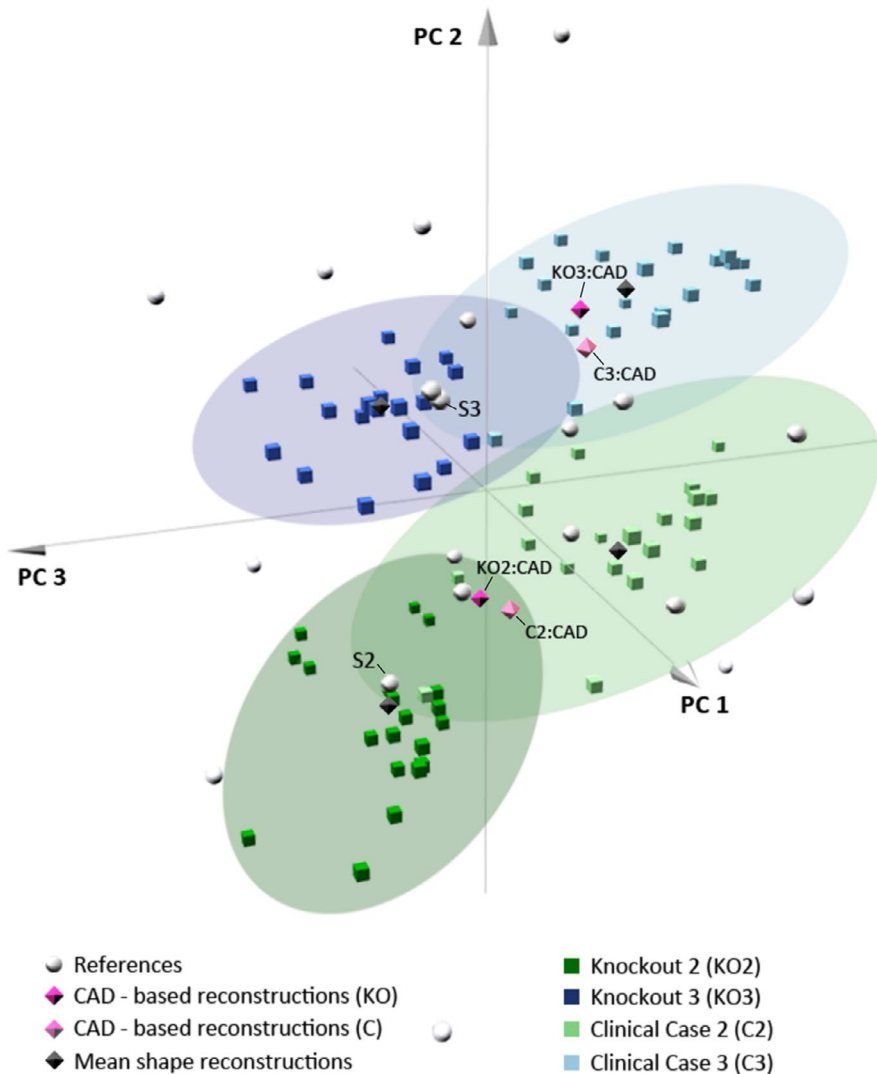
FIGURE 6 Principal component (PC) analysis plot showing the distribution of unilateral reconstructions (clinical cases: bright squares; knockout individual: dark-colored squares) projected into the reference shape-space (gray spheres). Reconstructions on the basis of the Procrustes mean shape (black diamond) plot closely to the reconstructed original specimens (S2 and S3). Computer-aided design (CAD)-based reconstructions (Materialise®) plot on the edge or outside the 95% confidence interval for KO2 and KO3 reconstruction (magenta diamond) and within the 95% confidence interval for C2 and C3 reconstructions (light magenta diamond) [Colour figure can be viewed at wileyonlinelibrary.com]

cranial defects. Shape variation in the reconstruction of C2 and C3 is slightly higher and shows a similar posterior distribution as the reconstruction of C1.

3.2 | Geometric accuracy

Using the complete reference cranium of the respective KO individual (i.e. S1 for the reconstruction of KO1, S2:KO2, S3:KO3), the TPS-based approach provides a very high accuracy with values <0.18 mm (see Table S1). RMSE for the reconstruction of KO1 with S1 is 0.0059 mm. For KO2 and KO3 the RMSE is 0.0032 and 0.1824 mm respectively. RMS errors using the reference sample range from 0.0850 to 0.5002 mm for KO1, 0.0789 to 0.64 mm for

KO2, and 0.0957 to 0.66 mm for KO3 (without RMSE for the reconstructions using the original, complete crania; see above). RMSE for the CAD-based reconstruction of KO1 is comparable to the TPS-based reconstruction (0.50 mm). However, accuracy of the CAD-based reconstructions for the lateral cases is significantly lower (KO2: 1.16 mm, KO3: 1.25 mm).

TPS-based mean shape reconstructions show a high accuracy and are located in the lower quartile in Figure 7. In contrast, all CAD−based reconstructions of KO1–KO3 show the lowest accuracy (upper whiskers in each boxplot; also see Table 1). The low interquartile range of KO1 points to a high reconstruction accuracy. In general, KO1 shows the smallest geometric deviations. The higher interquartile range for RMSE of KO2 and KO3 corresponds well with the elongated, elliptical clustering of reconstructions in the PCA plot (see Figure 5).
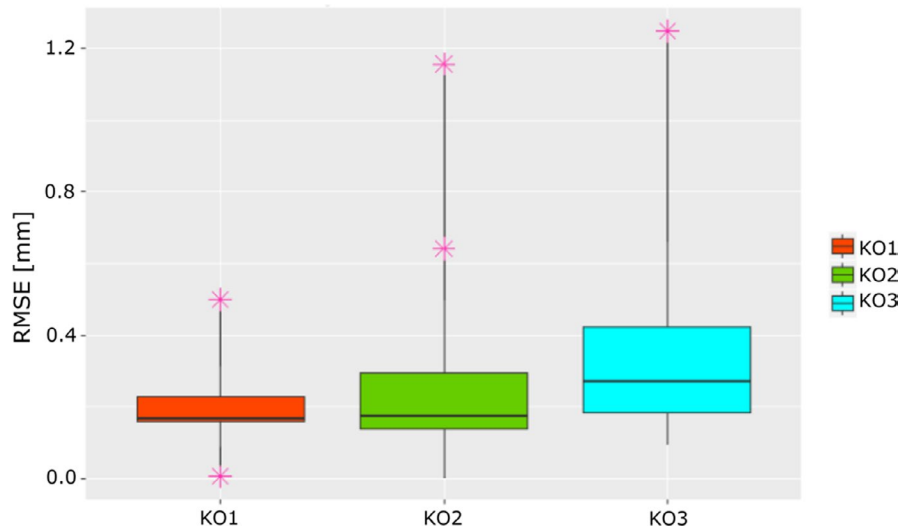
FIGURE 7 Root-mean-square error (RMSE) of implant geometric accuracy: (1) bilateral reconstructions show the lowest range and two outliers; (2) unilateral reconstructions show a higher variation and two outliers; (3) unilateral reconstructions are characterized by the largest variation and one outlier represented by the CAD-based reconstruction [Colour figure can be viewed at wileyonlinelibrary.com]
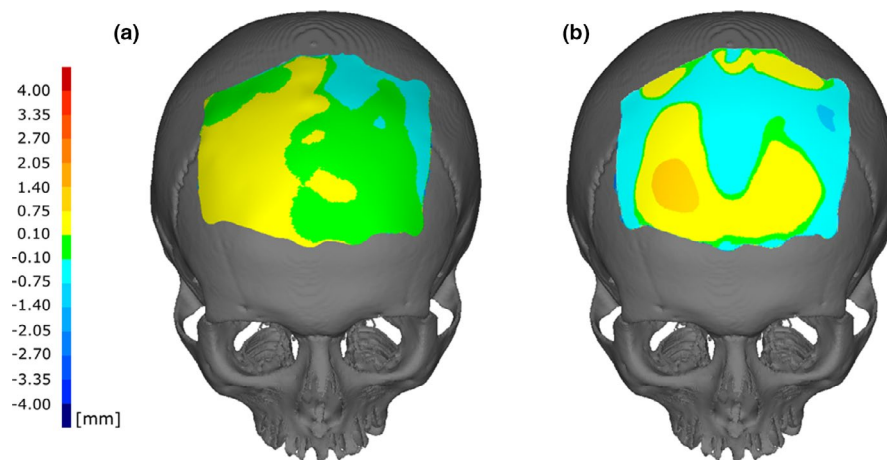

FIGURE 8 Geometric accuracy of the bilateral implant design (KO1): Nominal-actual comparison showing surface deviations between the original cranium and (a) thin-plate spline-based reconstruction using the Procrustes mean shape and, (b) the computer-aided design-based reconstruction in Materialise® [Colour figure can be viewed at wileyonlinelibrary.com]
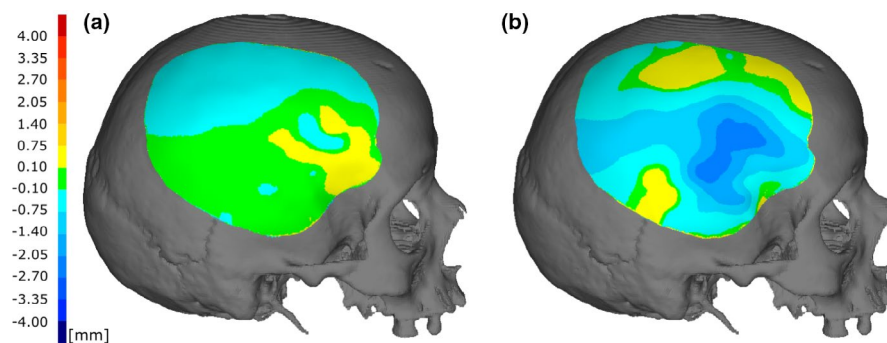

FIGURE 9 Geometric accuracy of the unilateral implant design (KO2): Nominal-actual comparison showing surface deviations between the original cranium and (a) thin-plate spline-based reconstruction using the Procrustes mean shape and, (b) the computer-aided design-based reconstruction in Materialise® [Colour figure can be viewed at wileyonlinelibrary.com]
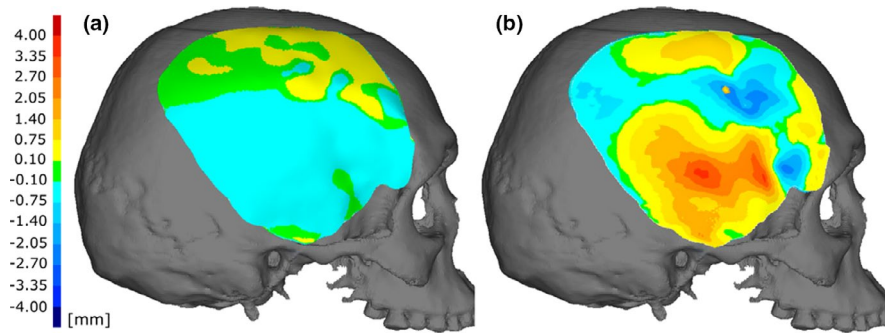
FIGURE 10 Geometric accuracy of the unilateral implant design (KO3): Nominal-actual comparison showing surface deviations between the original cranium and (a) thin-plate spline-based reconstruction using the Procrustes mean shape and, (b) the reconstruction in Materialise® [Colour figure can be viewed at wileyonlinelibrary.com]
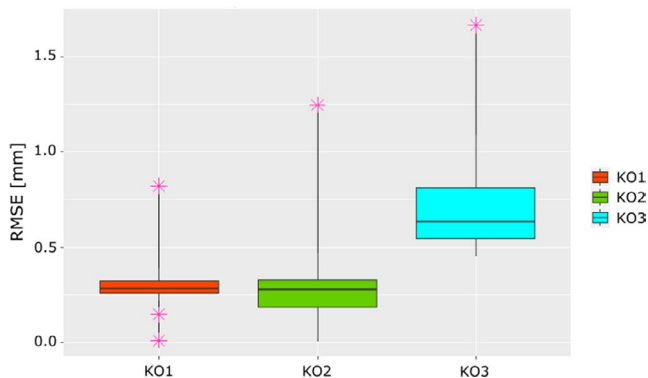

FIGURE 11 Root-mean-square error (RMSE) of implant thickness: (1) bilateral reconstruction with lowest range and three outliers; (2) unilateral reconstruction with increased range/variety and one outlier (computer-aided design [CAD]-based reconstruction); (3) unilateral reconstruction with biggest range and one outlier (CAD-based reconstruction) [Colour figure can be viewed at wileyonlinelibrary.com]

3.3 | Bilateral defect (KO1)

The TPS-based mean shape reconstruction of KO1 shows moderate positive and negative deviations in the analyzed implant area (Figure 8a). The reconstructed region shows a minor asymmetric pattern displaying higher values at the right *os frontale* and lower values in the parietal region. The frontal plane and small fractions around the bregma region in the CAD-based reconstruction (Figure 8b) are characterized by positive values indicating a strongly pronounced curvature of the reconstructed area of the forehead. Slightly negative values indicate reconstructed areas that are characterized by a decreased curvature, that is, flattened areas. In general, the high accuracy of the TPS-based reconstruction using the mean shape (values between ±0.75 mm) is reflected in the PCA, plotting close to the complete original specimen S1 (see Figure 4). The CAD-based reconstruction plots on the edge of the 95% interval in the PCA plot, reflecting lower accuracy as shown in Figure 8b.

3.4 | Unilateral defect (KO2)

The KO2 reconstruction shows a very high accuracy amongst all TPS-based mean shape reconstructions. The superior part of the implant is characterized by negative values transitioning into the parietal region showing very low deviations. Positive deviations are pronounced inferior to the temporal line at the height of the upper postorbital constriction (values between ±0.75 mm) (Figure 9a). The PCA plot in Figure 5 shows that the PMS reconstructions plots close to the original cranium S2. In comparison, the CAD-based reconstruction shows increased positive and negative deviations at the transition area of bone to implant (Figure 9b). The central part of the implant area is characterized by a high level of negative deviation showing peak values in the squamous part of the temporal bone. The result of the nominal- actual comparison is substantiated by the high RMSE of 1.16 mm, being significantly higher compared to the TPS-based reconstruction (RMSE: 0.08 mm). Additionally, the high RMSE of the CAD-based reconstruction is reflected in the respective PCA plot (Figure 4), the reconstruction plotting outside the 95% confidence interval along PC1 that is strongly influenced by cranial breadth, that is, the lateral parts of the cranium most affected by the large defect.

3.5 | Unilateral defect (KO3)

The PMS reconstruction in Figure 10a shows mainly negative deviations in the inferior two-thirds of the implant, that is, in the regions of the temporal and sphenoid bone. In the superior region that comprises parts of the parietal and frontal bone, the implant shows a slight positive deviation from the original cranium (values between ±0.75 mm). The CAD-based KO3 reconstruction is characterized by pronounced positive (os temporal and os sphenoid) and negative (temporal line) deviations, particularly in the region of the squamous part of the temporal bone. The RMSE of the CAD-based reconstruction is relatively high (1.25 mm; Table S1) supporting the result of the nominal-actual comparison. Both unilateral cases show the highest deviation in the area below the temporal line that is characterized
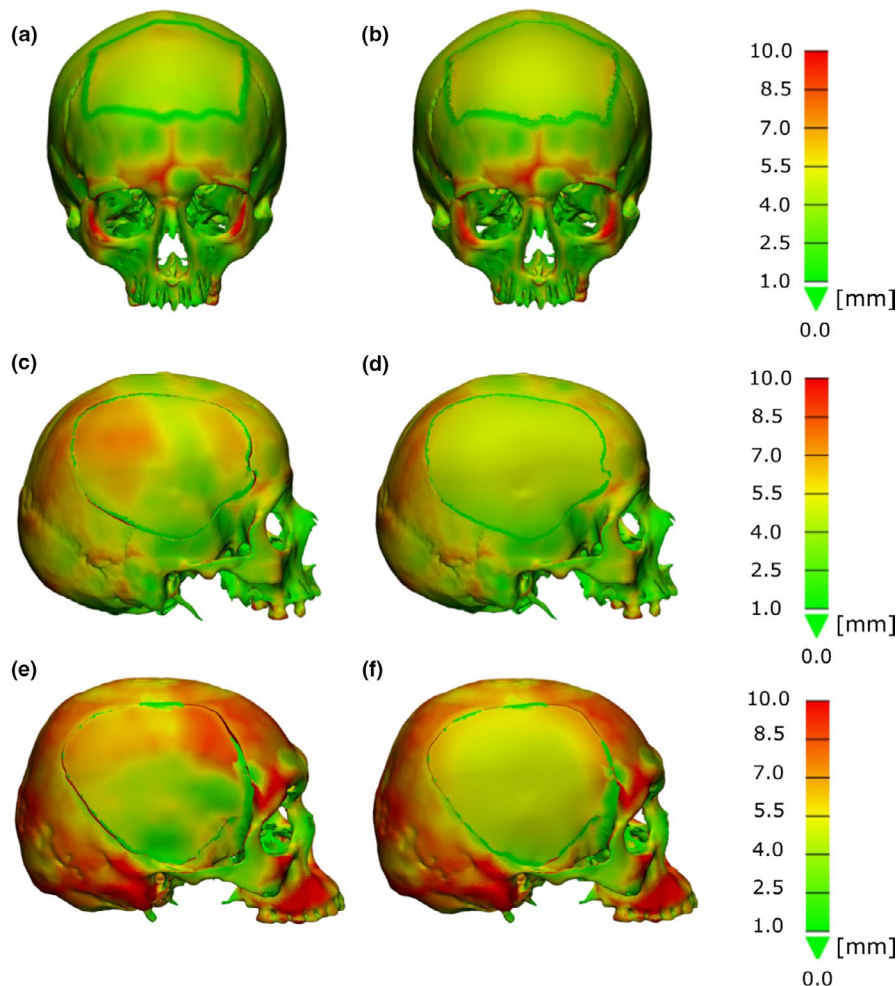
FIGURE 12 Wall thickness analysis in Materialise® comparing thin-plate spline-mean shape reconstruction and computer-aided design-based reconstruction (Materialise®) of KO1–KO3: (a) KO1 mean shape reconstruction, (b) KO1 Materialise® reconstruction, (c) KO2 mean shape reconstruction, (d) KO2 Materialise® reconstruction, (e) KO3 mean shape reconstruction, (f) KO3 Materialise® reconstruction [Colour figure can be viewed at wileyonlinelibrary.com]

by a more complex surface topography and a higher curvature, for example, in the regions of the postorbital constriction.

3.6 | Implant's thickness variation

Additionally, we performed wall thickness analyses for each virtual reconstruction, that is, generated cranial implant, in Materialise® to quantify the thickness accuracy of the investigated approaches. RMSE represents the deviations between the thickness of the original cranial bone and the thicknesses of virtually generated implant. A small RMSE represents a high accuracy. In the TPS- based reconstructions, using the original cranium provides an accuracy of 0.62 mm for KO1, 0.64 mm for KO2 and 0.71 mm for KO3. The RMSE for thickness accuracy in TPS-based reconstructions ranges from 0.64 to 1.09 mm for KO1, 0.63 to 0.91 mm for KO2 and 0.65 to 1.08 mm for KO3 when omitting the original, complete cranium. RMSE for the CAD-based reconstruction of KO1 (0.64 mm) is comparable to the TPS-based reconstruction using the PMS (0.69 mm).

However, accuracy of the CAD-based reconstructions for the lateral cases is significantly lower (KO2: 1.38 mm, KO3: 1.67 mm) compared to TPS-based reconstructions using the PMS (KO2: 0.63 mm, KO3: 0.70 mm).

The interquartile range of the RMSE of implant thickness in Figure 11 shows a similar pattern as shown for the geometric accuracy. PMS reconstructions are located in the lower quartile, while CAD-based reconstructions for the lateral cases KO2 and KO3 represent the maximum values in the respective boxplot (see Table S2). It is obvious that the implant thickness distribution of KO3—having the largest area to reconstruct—shows the lowest accuracy and highest standard deviation. The highest accuracy in terms of RMSE can be found for the bilateral reconstruction.

Figure 12a–f shows the TPS-based mean shape reconstructions from KO1 to KO3 on the left side and the corresponding CAD-based reconstructions on the right side. The most noticeable differences concern the local distribution of cranial bone thickness in the reconstructed areas. While the geometric reconstructions reproduce the bone thickness distribution that can be found in the original bone,

the reconstructions carried out in Materialise® show a rather uniform thickness distribution over the entire implant surface. While the differences in thickness distribution between the two reconstruction approaches is moderate in the bilateral case (C1:KO1), a major disagreement can be found in the cases with missing areas in the lateral cranial regions. Using the TPS-based approach, the patient-specific morphology of the missing cranial area, that is, parts of the parietal, frontal, sphenoid, and temporal bone, is estimated more accurately showing a smooth transition from thicker to thinner areas and a good agreement of bone thickness values at the border of the respective implant. Accordingly, a thicker bone in the posterior and superior aspects of the implant including parts of the parietal and frontal bone is reproduced more accurately in the TPS-based approach using the PMS as reference in KO2 (Figure 12c) and KO3 (Figure 12e).

4 | DISCUSSION

The use of CAS and virtual reconstruction techniques extensively increased in the last years, overcoming some problems inherent in traditional approaches, particularly in relation to reproducibility. This study investigates the accuracy of patient-specific cranial implants and compares the outcome of two different reconstruction approaches: CAD-based and TPS-based using a reference sample and TPS warping. In contrast to earlier investigations, we additionally quantified the accuracy in relation to implant thickness of digitally designed cranial flaps in three realistic clinical cases showing large uni- and bilateral defects.

4.1 | CAD versus TPS-based approach

Because every reconstruction relies on assumptions of missing data, it is impossible to achieve a perfect original state. Reconstructions are therefore only approximations towards the original state, e.g. based on anatomical information from undamaged individuals (Gunz et al., 2009). In this study, we used two different but not exclusive approaches for missing data estimation for large cranial defects. Implants designed with a CAD-based approach using a commercially available software package commonly used for cranial reconstructions (Materialise®) show a moderate to high geometric accuracy in this analysis. However, the accuracy was considerably lower for large unilateral defects compared to reconstructions from the TPS-based approach, e.g. using the PMS as template. The overall accuracy in terms of RMSE is comparable to earlier studies (Halazonetis, 2001; Hassan et al., 2017; Hazeveld et al., 2014; Schirmer & Wiltshire, 1997; Sohmura et al., 2001) for both approaches. However, the TPS-based approach has two main advantages: (1) accuracy is higher for the estimation of missing areas in anatomic regions characterized by a complex topology, for example, the sphenoid region, and (2) it provides implants whose thickness distribution reproduces the variation in the original bone with a high accuracy (RMSE <0.70 mm

using the PMS). Implants with a variable thickness can be produced using AM or molding and may be advantageous in the distribution of peak stresses due the ability to mimic bones biomechanical behavior more adequately.

The major advantage of the CAD-based approach is its time effectiveness applying a straightforward, semi-automatic sequence of steps involving CT data processing, mirror imaging techniques and splines, and post-processing, for example, undercut removal and edge smoothing. This allows the design of implants based on individual patient data because only the respective STL geometry and shape of the splines have to be adapted. Experienced personnel will perform several reconstructions on a working day. In contrast, the TPS-based approach is more time-consuming because a landmark template has to be defined a priori, ideally optimized for each implant morphology separately including data on the internal and external aspects of the cranium. Depending on the reference for reconstruction, either the PMS or other complete crania that are warped onto the clinical case showing cranial defects are necessary. The placement of anatomical landmarks and curved landmarks need to be placed manually for each template which necessitates expert anatomical knowledge. However, once finalized an appropriate template can be saved and used for similar future cases significantly decreasing the amount of effort. In total, this approach takes approximately twice as much time for an implant reconstruction if carried out by a trained person. However, recent digitization efforts in relation to (semi-)automated image segmentation, registration, and landmark placement, for example, using machine learning, may help to overcome this limitation and produce landmark configurations as anatomically precise as expert manual annotations (Percival et al., 2019). Ultimately, this will significantly decrease the lead-time for implant generations using a TPS-based approach. Statistical shape models (SSM) provide another powerful alternative for fast and semi-automated computer-assisted surgical procedures that have the potential to overcome restrictions inherent in TPS- and CAD-based approaches, for example, in relation to automation capabilities, high-costs, and lead-time. SSM employ aligned surface meshes from a training data set and parametrize shape by performing a PCA. Additionally, missing information due to poor CT image quality, for example, because of beam-hardening artifacts, can be interpolated by SSM (Semper-Hogg et al., 2017).

To prevent a competitive disadvantage in the CAD-based approach and to be able to directly compare the reconstruction outcomes in our analyses, we used the geometrical information of the PMS, that is, the curvature of the external bone surface, during the CAD-based reconstruction of the bilateral case (C1:KO1; see Figure 2). Either way, the relevant anatomical information in this approach is limited to the cranial part directly below the drawn splines which have to be adjusted manually (see Figure 2). The implant margin is determined by a manually drawn curve that surrounds the defect. These two parameters, as well as implant thickness, are the basic input for the CAD-based virtual implant design in Materialise®. However, this approach does not include information for the creation of the internal implant surface. Using the command "variable

offset" it is only possible to manually measure thickness values on the outer surface, which are then subsequently applied to the inner surface. Hence, implants created in Materialise® using the dedicated implant creation workflow (Materialise, 2018) show a homogeneous thickness distribution if additional information is unavailable, that is, the topology of the outer and inner surface is very similar (see Figure 12).

In contrast, TPS-based reconstructions employ the anatomical information of a reference specimen (e.g. the PMS or a geometrically similar specimen) or a sample of reference specimen to create a posterior distribution of several reconstructions. This approach incorporates an inherent pre-alignment on the basis of defined anatomical landmarks and estimates missing data using TPS. This approach is well suited for the reconstruction of large missing areas characterized by a smooth curvature like in the neurocranium (Senck et al., 2013). Using the PMS for reconstruction minimizes the effect of incorporating the morphology of the reference in the final reconstruction outcome. However, a precondition for the TPS-based approach is a feasible landmark template that densely samples the defect region—particularly the edges of the missing area. In this analysis, the landmark template covers the complete external and internal aspects of the affected cranial surface. This allows—in contrast to the described CAD-approach—to model an implant with a variable thickness distribution. While a smooth perimeter of the defective regions leads to a smooth transition of the remaining bone to the implant, small curvatures or a complex topology around the edges can lead to an increased uncertainty (Senck et al., 2015). Since the neurocranial missing areas in the described cases show smooth edges, it is possible to generate implants that are well adapted to the cranial surface of the large missing areas. Nevertheless, the cranial geometry and bone thickness of the reference are incorporated into the final implant. Hence, it is preferable to use the PMS during reconstruction to minimize the influence of the reference choice during virtual reconstruction (Senck et al., 2015).

4.2 | Reconstruction accuracy

The RMSE of each TPS-based mean shape reconstruction is below 0.18 mm (Table S1), as shown in the KO analyses simulating three clinically relevant cases (KO1, KO2, and KO3). All KO1 reconstructions cluster closely around the original cranium (S1) in the PCA plot (see Figure 5) within the 95% confidence interval. While the PMS reconstruction shows a high accuracy (RMSE: 0.16 mm), the CAD—based reconstruction shows the lowest accuracy (RMSE: 0.50 mm). The CAD-based reconstruction of KO1 is characterized by a more pronounced curvature of the forehead, while the surrounding areas are flattened (see Figure 9b). Using Materialise®, it is advantageous to take a complete cranium as reference, particularly to define the spline in the midsaggital plane since mirror imaging is not possible. The definition of the points that span the spline and the applied reference cranium determine the shape of the resulting virtual implant. In contrast, TPS takes the smoothness properties of the area

surrounding the region into account and is locally bent according to the surrounding morphology (Gunz et al., 2009). TPS is usually explained as a "smoothing" or "interpolation" function, which minimizes the overall bending energy of the map (Bookstein, 1991). The dense and evenly distributed landmarks over the internal and external cranial table guide the reconstruction of large cranial defects. In this study, we added additional curve semilandmarks in the midsagittal plane to increase the information available for the cranial reconstruction, supporting the geometric accuracy and the restoration of the cranial thickness. Since the used KO specimen (KO1) is characterized by a small degree of asymmetry, the reconstructed area shows some asymmetry along the midsagittal plane as well. Senck et al. (2015) showed that the choice of the reference but also the morphology of the specimen that is reconstructed, e.g. in relation to cranial asymmetry, govern the resulting geometry of the estimated missing area.

The posterior distribution of TPS-based reconstructions of KO2 and KO3 in the PCA shows that the main shape variations are along PC2 and PC3 (Figure 5), which reflect anatomical variation in cranial breadth including the temporal line and the degree of postorbital constriction (Figure 6). Both TPS-based mean shape reconstructions plot close to the respective original cranium in the KO analysis (S2 and S2 respectively), reflecting the high accuracy in terms of RMSE for both reconstructions (KO2: 0.07 mm, KO3: 0.18 mm; see Table S1). The high accuracy is also obvious in the nominal-actual comparisons in Figures 9 and 10. The dense landmark distribution as well as the additional digitization of the temporal line using curved semilandmarks supports the reconstruction outcome of the TPS-based approach. Figures 10a and 11a show low deviations in the nominal-actual comparison and an accurate temporal line restoration.

In contrast, both unilateral CAD-based reconstructions show a significantly lower accuracy (RMSE for KO2: 1.16 mm, KO3: 1.25 mm). CAD-based reconstructions show a depression along or below the temporal line. For KO2 (Figure 10b) the area of the *sphenoid* bone shows negative values (indentation), while KO3 (Figure 11b) shows high positive values in this area in the nominal-actual comparison (convex shaped). The increased reconstruction uncertainty for KO2 and KO3 is reflected in the interquartile range and the RMSE values of the CAD-based reconstructions with 1.16 and 1.25 mm (Table S2; Figure 7). Since the respective mirror image from the undamaged side serves as reference for CAD reconstructions, the results are biased by the natural cranial asymmetry (Metzger et al., 2007) which also influences implant geometry. Analogous to the CAD-based reconstruction of the bilateral case, the mirrored image has to be manually aligned with the KO individual in order to define splines determining the implant's shape—representing a major error source for the missing data estimation.

Fuessinger et al. (2018) reconstructed a virtually damaged cranium using GM (considering 6 anatomical landmarks) and compared this to the mirroring technique. The achieved reconstruction accuracy was 0.47 mm for the statistical mean shape reconstruction while the mirror-imaging technique yields an error of 1.13 mm. Benazzi and Senck (2011) reported a similar trend of obtaining lower

error values using the TPS-based method and higher values when using the mirroring technique. A similar investigation was carried out by Semper-Hogg et al. (2017), comparing mirroring technique with a landmark-guided approach using a SSM to reconstruct bony defects of the right zygoma. They report a mean deviation of 1.10 ± 0.23 mm for the mirroring approach and 0.85 ± 0.26 mm for the landmark guided method. Including more (anatomical) landmarks and a dense sampling of surface semilandmarks at the edges of defects will generally result in more accurate reconstructions, as shown in this analysis.

4.3 | Thickness accuracy

Analogous to the geometric accuracy, implant thickness accuracy decreases from KO1 (smaller defect area, homogenous topography) to KO3 (larger defect area, complex topography), also indicated by the increasing interquartile range (Figure 11). All Materialise® reconstructions are at the upper limit for RMSE values (Table S2). KO1 reconstruction shows the highest accuracy with a RMSE of 0.64 mm among the CAD-based reconstructions. The unilateral cases (KO2 and KO3) show higher RMSE of 1.38 and 1.67 mm respectively (Table S2). The wall thickness analyses of KO1–KO3 clearly display the differences in the resulting implants of the two approaches (Figure 12). Implant thickness at the transition area of bone and implant for the CAD-based reconstructions is merely determined by manually measured thickness values around the defect. Hence, all implants show a uniform thickness distribution without the consideration of the varying bone thickness distribution in the normal crania. In contrast, the TPS-based mean shape reconstructions take the surrounding bone thicknesses at the bone–implant transition area into account. Using TPS, we showed that the cranial thickness distribution can be restored with high accuracy even for geometrically challenging areas, for example, the *sphenoidal* region in the unilateral cases, since the thickness distribution of the reference (e.g. the PMS) is adopted in the specimen that is reconstructed.

In general, each cranial bone is characterized by an inherent variation in bone thickness dictated by genetic and functional aspects. Moreover, the distribution of bone thickness varies between different patients, for example, between KO2 and KO3 (see Figure 12), leading to an inadequate estimate of implant thickness when applying a uniform thickening approach on the basis of the external bone surface during a CAD-based reconstruction. According to Marcián et al. (2019), implant thickness is the most significant factor affecting stresses in implants. Additionally, it affects the implant deflection as well as Young's modulus of the implant material. By comparing different implant materials with different thicknesses the authors showed that an increasing implant thickness can be more advantageous than changing the implant material considering maximum von Mises stresses. For a change in implant deflection, the choice of the material has a slightly higher effect compared to the thickness, which has to be considered when using the generated virtual implants in subsequent (additive) manufacturing processes. The reported accuracy values are also relevant to estimate the total deviation of the produced implants, since production tolerances vary between different manufacturing processes. In particular, additive manufactured implants can show large tolerances (Chamo et al., 2020) that have to be added to the uncertainty of virtual implant generation to account for deviations that may have to be corrected for by the medical engineer or surgeon before the surgical procedure.

The high accuracy of reconstructions using the PMS leads us to the recommendation to use the mean shape to reconstruct extensive uni- and bilateral craniofacial defects. The PMS represents a population average shape thus minimizing the incorporation of reference specific traits in the final implant. Additionally the PMS shows a lower degree of asymmetry in comparison to single reference specimen (Benazzi & Senck, 2011). Further studies showed similar outcomes when using the PMS in the reconstruction of cranial defects in various primate species (Senck et al., 2015) and in large missing cranial regions (Senck et al., 2013). However, there is no exclusive method or reference for bone reconstruction since each outcome depends on the specific case under study. The accuracy of each generated implant is influenced by cranial shape and the size of the area that is reconstructed. Further studies are needed to explore if this recommendation also holds for implants in geometrically complex regions, for example, in the orbital region.

In a next step, we will additively manufacture all virtually created cranial flaps from PEEK and scan these implants using micro-CT to determine the uncertainty related to the manufacturing process. This will provide a measure for the total deviation between the virtual model and real implant. Finally, practical consequences for the neurosurgical procedure will be evaluated in the context of a subsequent clinical study.

5 | CONCLUSION

We showed that both approaches, TPS-based and CAD-based using Materialise®, are capable of reconstructing large unilateral and bilateral cranial defects with an RMSE of <1.25 mm. However, the TPS-based reconstruction approach is additionally able to reproduce implant thickness with a high accuracy using a dense distribution of internal and external landmarks across the neurocranium. Using existing landmark templates can significantly decrease the amount of time that has to be invested for the reconstruction of future clinical cases with cranial defects. In contrast, the CAD-based approach uses the geometric information of only one reference below a manually defined spline, which makes it fast but prone to deviations during alignment and mirror imaging. Also, implant thickness cannot mimic the physiological thickness distribution of the affected cranial bone adequately. Both approaches are well documented, hence increasing reproducibility when applying the reconstruction process step-by-step. The estimation of implant design accuracy is an important factor in the assessment of error propagation during implant manufacturing, particularly when using additive manufacturing.

AUTHOR CONTRIBUTION

C. Wittner carried out the reconstructions and participated in the drafting of the manuscript. M. Borowski and L. Pirl participated in data acquisition. J. Kastner, A. Schrempf, U. Schäfer, and K. Trieb provided a critical revision of the manuscript. S. Senck provided the concept, designed the reconstruction protocols and participated in the drafting of the manuscript.

DATA AVAILABILITY STATEMENT

The data that support the findings of this study are available from the corresponding author, Sascha Senck, upon reasonable request.

ORCID

Sascha Senck 🄳 https://orcid.org/0000-0001-8400-5121

REFERENCES

Benazzi, S. & Senck, S. (2011) Comparing 3-dimensional virtual methods for reconstruction in craniomaxillofacial surgery. *American Association of Oral and Maxillofacial Surgeons*, 69, 1184–1194.

Bonda, D.J., Manjila, S., Selman, W.R. & Dean, D. (2015) The recent revolution in the design and manufacture of cranial implants: modern advancements and future directions. *Neurosurgery*, 77(5), 814–824.

Bookstein, F.L. (1989) Principal warps: thin-plate splines and the decomposition of deformations. *IEEE Transactions on Pattern Analysis and Machine Intelligence*, 11(6), 567–585.

Bookstein, F.L. (1991) *'Morphometric tools for landmark data geometric and biology.* Cambridge: Cambridge University.

Bookstein, F.L. & Green, W.D.K. (1993) A feature space for edgels in images with landmarks. *Journal of Mathematical Imaging and Vision*, 3(3), 231–261. https://doi.org/10.1007/bf01248355.

Bookstein, F.L. & Green, W.D.K. (1994) Edgewarp: a flexible program package for biometric image warping in two dimensions. *Proc. SPIE: 2359, Visualization in Biomedical Computing*, 2359. https://doi.org/10.1117/12.185174

Brown, G.B., Currier, G.F., Kadioglu, O. & Kierl, J.P. (2018) Accuracy of 3-dimensional printed dental models reconstructed from digital intraoral impressions. *American Journal of Orthodontics and Dentofacial Orthopedics*, 154(5), 733–739. https://doi.org/10.1016/j.ajodo.2018.06.009.

Chamo, D., Msallem, B., Sharma, N., Aghlmandi, S., Kunz, C. & Thieringer, F.M. (2020) Accuracy assessment of molded, patient-specific polymethylmethacrylate craniofacial implants compared to their 3D printed originals. *Journal of Clinical Medicine*, 9(3), 832. https://doi.org/10.3390/jcm9030832.

Egger, J., Gall, M., Tax, A., Üçal, M., Zefferer, U., Li, X. et al. (2017) Interactive reconstructions of cranial 3D implants under MeVisLab as an alternative to commercial planning software. *PLoS One*. https://doi.org/10.1371/journal.pone.0172694.

Fröhler, B., Weissenböck, J., Schiwarth, M., Kastner, J. & Heinzl, C. (2019) open_iA: A tool for processing and visual analysis of industrial computed tomography datasets. *Journal of Open Source*. https://doi.org/10.1111/cgf.12896.

Fuessinger, M.A., Schwarz, S., Cornelius, C.-P., Metzger, M.C., Ellis, E., Probst, F. et al. (2018) Planning of skull reconstruction based on a statistical shape model combined with geometric morphometrics. *International Journal of Computer Assisted Radiology and Surgery*, 13(4), 519–529. https://doi.org/10.1007/s11548-017-1674-6.

Gunz, P., Mitteroecker, P., Neubauer, S., Weber, G.W. & Bookstein, F.L. (2009) Principles for the virtual reconstruction of hominin crania. *Journal of Human Evolution*, 57(1), 48–62. https://doi.org/10.1016/j.jhevol.2009.04.004.

Halazonetis, D.J. (2001) Acquisition of 3-dimensional shapes from images. *American Journal of Orthodontics and Dentofacial Orthopedics*, 119(5), 556–560. https://doi.org/10.1067/mod.2001.115459.

Hassan, S., Xue, L., Anh, J., Pakala, M., Sin, G. & Okazaki, M. (2017) STT-RAM device performance improvement using CMP process. In 2017 28th Annual SEMI Advanced Semiconductor Manufacturing Conference (ASMC), pp. 209–211. https://doi.org/10.1109/asmc.2017.7969231.

Hazeveld, A., Huddleston Slater, J.J.R. & Ren, Y. (2014) Accuracy and reproducibility of dental replica models reconstructed by different rapid prototyping techniques. *American Journal of Orthodontics and Dentofacial Orthopedics*, 145(1), 108–115. https://doi.org/10.1016/j.ajodo.2013.05.011.

Jones, R.H.B. (2013) The use of virtual planning and navigation in the treatment of temporomandibular joint ankylosis. *Australian Dental Journal*, 58(3), 358–436. https://doi.org/10.1111/adj.12086.

Klammert, U., Gbureck, U., Vorndran, E., Rödiger, J., Meyer-Marcotty, P. & Kübler, A.C. (2010) 3D powder printed calcium phosphate implants for reconstruction of cranial and maxillofacial defects. *Journal of Cranio-Maxillofacial Surgery*, 38(8), 565–570. https://doi.org/10.1016/j.jcms.2010.01.009.

Kwarcinski, J., Boughton, P., Ruys, A., Doolan, A. & van Gelder, J. (2017) Cranioplasty and craniofacial reconstruction: a review of implant material, manufacturing method and infection risk. *Applied Sciences*, 7(3), 276. https://doi.org/10.3390/app7030276.

Ladaru, A., Moisa, H. & Ciurea, A.V. (2019) 3D patient specific implants for cranioplasty. *Romanian Neurosurgery*, 277–282. https://doi.org/10.33962/roneuro-2019-046.

Marcián, P., Narra, N., Borák, L., Chamrad, J. & Wolff, J. (2019) Biomechanical performance of cranial implants with different thicknesses and material properties: a finite element study. *Computers in Biology and Medicine*, 109, 43–52. https://doi.org/10.1016/j.compbiomed.2019.04.016.

Marreiros, F.M.M., Heuzé, Y., Verius, M., Unterhofer, C., Freysinger, W. & Recheis, W. (2016) Custom implant design for large cranial defects. *International Journal of Computer Assisted Radiology and Surgery*, 11(12), 2217–2230. https://doi.org/10.1007/s11548-016-1454-8.

Materialise. (2018) *Mimics innovation suite training guide.* Wien. Available at: https://www.materialise.com/de/events/medical/mimics-innovation-course-vienna [Accessed 21th Nov 2018].

Metzger, M.C., Hohlweg-Majert, B., Schön, R., Teschner, M., Gellrich, N.-C., Schmelzeisen, R. et al. (2007) Verification of clinical precision after computer-aided reconstruction in craniomaxillofacial surgery. *Oral Surgery, Oral Medicine, Oral Pathology, Oral Radiology and Endodontology*, 104(4), 1–10. https://doi.org/10.1016/j.tripleo.2007.04.015.

Mitteroecker, P. & Gunz, P. (2009) Advances in geometric morphometrics. *Evolutionary Biology*, 36(2), 235–247. https://doi.org/10.1007/s11692-009-9055-x.

Mohan, D. (2016) Current implants used in cranioplasty. In: *Handbook of bioceramics and biocomposites*. Springer International Publishing, pp. 1275–1307. https://doi.org/10.1007/978-3-319-12460-5_59.

Moiduddin, K., Darwish, S., Al-Ahmari, A., ElWatidy, S., Mohammad, A. & Ameen, W. (2017) Structural and mechanical characterization of custom design cranial implant created using additive manufacturing. *Electronic Journal of Biotechnology*, 29, 22–31. https://doi.org/10.1016/j.ejbt.2017.06.005.

Mokri, B. (2010) Orthostatic headaches in the syndrome of the trephined: Resolution following cranioplasty. *Headache*, 50(7), 1206–2121. https://doi.org/10.1111/j.1526-4610.2010.01715.x.

Msallem, B., Beiglboeck, F., Honigmann, P., Jaquiéry, C. & Thieringer, F. (2017) Craniofacial reconstruction by a cost-efficient template-based process using 3D printing. *Plastic and Reconstructive Surgery—Global Open*, 5(11), 1–5. https://doi.org/10.1097/GOX.0000000000001582.

Percival, C.J., Devine, J., Darwin, B.C., Liu, W., Eede, M., Henkelman, R.M. et al. (2019) The effect of automated landmark identification on morphometric analyses. *Journal of Anatomy*, 234(6), 917–935. https://doi.org/10.1111/joa.12973.

Persson, J., Helgason, B., Engqvist, H., Ferguson, S.J. & Persson, C. (2018) Stiffness and strength of cranioplastic implant systems in comparison to cranial bone. *Journal of Cranio-Maxillofacial Surgery*. https://doi.org/10.1016/j.jcms.2017.11.025.

Petersmann, S., Spoerk, M., Huber, P., Lang, M., Pinter, G. & Arbeiter, F. (2019) Impact optimization of 3D-printed poly(methyl methacrylate) for cranial implants. *Macromolecular Materials and Engineering*, 304, 1900263. https://doi.org/10.1002/mame.201900263.

Quinto-Sánchez, M., Adhikari, K., Acuña-Alonzo, V., Cintas, C., Silva de Cerqueira, C.C., Ramallo, V. et al. (2015) Facial asymmetry and genetic ancestry in Latin American admixed populations. *American Journal of Physical Anthropology*, 157(1), 58–70. https://doi.org/10.1002/ajpa.22688.

R Core Team. (2013) *R: a language and environment for statistical computation*. Vienna, Austria: R Foundation for Statistical Computing.

Rotaru, H., Stan, H., Florian, I.S., Schumacher, R., Park, Y.-T., Kim, S.-G. et al. (2012) Cranioplasty with custom-made implants: Analyzing the cases of 10 patients. *Journal of Oral and Maxillofacial Surgery*, 70(2), 169–176. https://doi.org/10.1016/j.joms.2011.09.036.

Schirmer, U.R. & Wiltshire, W.A. (1997) Manual and computer-aided space analysis: a comparative study. *American Journal of Orthodontics and Dentofacial Orthopedics*, 112(6), 676–680. https://doi.org/10.1016/S0889-5406(97)70234-8.

Schlager, S. (2017) Morpho and Rvcg—shape analysis in R: R-packages for geometric morphometrics, shape analysis and surface manipulations. In: *Statistical shape and deformation analysis*. pp. 217–256. https://doi.org/10.1016/B978-0-12-810493-4.00011-0.

Semper-Hogg, W., Fuessinger, M.A., Schwarz, S., Ellis, E., Cornelius, C.-P., Probst, F. et al. (2017) Virtual reconstruction of midface defects using statistical shape models. *Journal of Cranio-Maxillofacial Surgery*, 45(4), 461–466. https://doi.org/10.1016/j.jcms.2016.12.020.

Senck, S., Bookstein, F.L., Benazzi, S., Kastner, J. & Weber, G.W. (2015) Virtual reconstruction of modern and fossil hominoid crania: consequences of reference sample choice. *Anatomical Record*, 298(5), 827–841. https://doi.org/10.1002/ar.23104.

Senck, S., Coquerelle, M., Weber, G.W. & Benazzi, S. (2013) Virtual reconstruction of very large skull defects featuring partly and completely missing midsagittal planes. *Anatomical Record*, 296(5), 745–758. https://doi.org/10.1002/ar.22693.

Singare, S., Lian, Q., Ping Wang, W., Wang, J., Liu, Y., Li, D. et al. (2009) Rapid prototyping assisted surgery planning and custom implant design. *Rapid Prototyping Journal*, 15(1), 19–23. https://doi.org/10.1108/13552540910925027.

Sohmura, T., Hirogaki, Y., Satoh, H., Takahashi, J. & Takada, K. (2001) Complete 3-d reconstruction of dental cast shape using perceptual grouping. *IEEE Transactions on Medical Imaging*, 20(10), 1093–1101. https://doi.org/10.1109/42.959306.

Truscott, M., de Beer, D., Vicatos, G., Hosking, K., Barnard, L., Booysen, G. et al. (2007) Using RP to promote collaborative design of customised medical implants. *Rapid Prototyping Journal*, 13(2), 107–114. https://doi.org/10.1108/13552540710736795.

Wittner, C. (2019) Reconstruction of uni- and bilateral cranial defects using deformation-based morphometrics to generate patient-specific implants. Master thesis, University of Applied Sciences Upper Austria Linz.

Zachow, S. (2015) Computational planning in facial surgery. *Facial Plastic Surgery*, 31(5), 446–462. https://doi.org/10.1055/s-0035-1564717.

SUPPORTING INFORMATION

Additional supporting information may be found online in the Supporting Information section.